Nanoscale Advances

ROYAL SOCIETY OF CHEMISTRY

PAPER

View Article Online
View Journal | View Issue

Cite this: *Nanoscale Adv.*, 2025, **7**, 2942

A novel 3D Fe_2O_3@$ZnBi_2O_4$ n–p heterojunction with high photocatalytic activity under visible light

Thi Viet Ha Luu, *[a] Van Cuong Nguyen, [a] Thi Dieu Thuy Tran,[a] Van Dat Doan, [a] Thi Lieu Nguyen,[a] Nguyen Xuan Dung[b] and Huu Phuc Dang *[c]

A novel n–p Fe_2O_3@$ZnBi_2O_4$ (FZB) heterojunction with a unique 3D structure was fabricated in two simple steps to break down MB under visible light. First, the polymer gel combustion technique was employed to fabricate a 3D Fe_2O_3 framework. Next, a microwave-assisted precipitation approach was used to incorporate 3D $ZnBi_2O_4$ flakes onto the framework surface. FZB can effectively collect a broad range of UV-Vis light and sunlight. Surprisingly, the core–shell p–n heterojunction structure makes it easier for photogenerated charges to move and separate. This is because the semiconductor parts are better connected and the electric field is inside the two junctions. UV-Vis-DRS, EIS, PL, and XPS analyses confirmed this phenomenon. As a result, n–p FZB, with a Fe_2O_3/$ZnBi_2O_4$ molar ratio of 2 : 1, showed the highest photocatalytic activity, increasing the reaction rate by 4.2 times compared to Fe_2O_3 and 2.8 times compared to $ZnBi_2O_4$. Exposure to light for 100 min at a concentration of 0.7 g L^{-1} the FZB catalyst and pH = 9 led to the breakdown of more than 95% of the 50 ppm MB solution. In addition, the photodegradation of MB by n–p FZB increased the reaction rate by 2.15 times by adding hydrogen peroxide (H_2O_2), which is known as the photo-Fenton reaction. The efficacy showed remarkable photocatalytic activity, which increased the reaction rate by 5.95 times when persulfate was used. Finally, after examination of the energy band structure of the materials and the findings regarding the function of the oxidizing sites in the photocatalytic process, a reaction mechanism was proposed.

Received 13th December 2024
Accepted 26th February 2025

DOI: 10.1039/d4na01039f

rsc.li/nanoscale-advances

1. Introduction

The rapid growth of global industrialization has led to an increase in the demand for water resources. Moreover, industrial, agricultural, and urban regions release a substantial amount of garbage (approximately 2 million tons) into the environment daily, endangering human health and increasing the risk of water resource depletion. Industrial wastewater, which frequently contains numerous hazardous organic compounds, is challenging to break down and exhibits significant biological toxicity. Currently, more than 100 000 varieties of dyes are used in diverse textile manufacturing procedures. The majority of dyes, including rhodamine B (RhB), methyl orange (MO), and methylene blue (MB), are soluble in water, have low biodegradability, and pose potential risks to ecosystems.[1] Approximately 13% of the global population is already experiencing water scarcity, and this figure is projected to increase to 40% by the 2050s.[2] Thus, the global issue lies in discovering practical solutions for water treatment and recycling technologies that are environmentally benign, cost-effective, and highly efficient.[3]

Advanced oxidation uses highly reactive oxidizing agents to break down and remove organic pollutants from water or air. Studies have demonstrated that Advanced Oxidation Processes (AOPs) are efficient techniques for converting harmful organic pollutants into minerals and for eliminating contaminants from wastewater. Advanced oxidation processes (AOPs) that use $^{\bullet}OH$ radicals (which have a standard electrode potential of 2.80 V/SHE) are very strong oxidizing agents that do not care what they are attacking. They can efficiently convert organic contaminants present in water into harmless smaller molecules such as CO_2 and H_2O.[3–6] Photocatalysis, typically using UV-Vis light, generates $^{\bullet}OH$ radicals. Advanced oxidation techniques have been used in the textile, pharmaceutical, printing, and pulp industries to treat wastewater.[3,7,8] However, this technology is still in use. In practice, photocatalytic technology still has limitations in terms of quantum efficiency, durability, and catalyst cost. In the majority of individual semiconductor photocatalysts, the pace at which the photoelectron–hole pairs recombine is rapid, resulting in low quantum efficiency and performance.[9,10] Several widely recognized semiconductors exhibit excellent photocatalytic activities owing to their large bandgap energies. UV radiation specifically activates TiO_2, ZnO,

[a]Faculty of Chemical Engineering, Industrial University of Ho Chi Minh City, No. 12 Nguyen Van Bao, Ward 1, Go Vap District, Ho Chi Minh City, 700000, Vietnam. E-mail: luuthivietha@iuh.edu.vn

[b]Vinh University, 182 Le Duan, Vinh City, Nghe An, 460000, Vietnam

[c]Faculty of Fundamental Science, Industrial University of Ho Chi Minh City, No. 12 Nguyen Van Bao, Ward 1, Go Vap District, Ho Chi Minh City, 700000, Vietnam. E-mail: danghuuphuc@iuh.edu.vn

CeO_2, and SnO_2. Consequently, their spectral response range is limited, preventing the effective absorption of sunlight, particularly visible light.[11–13] Sulfide and nitride semiconductors have band gap energies in the visible range; however, they are not very stable and do not last long in wet environments.[14] Hence, it is imperative to address the aforementioned constraints by creating novel semiconductor materials derived from conventional semiconductors.

Hematite, also known as Fe_2O_3, is a semiconductor that exhibits n-type conductivity and has a band gap energy ranging from approximately 2.0 to 2.2 electron volts (eV). Hematite can capture light ranging from yellow to ultraviolet, specifically at a wavelength of $\lambda \leq 600$ nm. It can absorb up to 40% of the energy in the solar spectrum. In addition, hematite exhibits favorable environmental characteristics, demonstrates excellent stability in aqueous solutions with pH greater than 3, and is among the most cost-effective options for semiconductor materials.[14–16] Thus, hematite is a highly intriguing choice for photocatalytic applications that specifically aim to harness visible light, particularly sunlight.[17] Nevertheless, certain characteristics, such as the rapid recombination rate of electrons and holes, the limited diffusion length of holes (2–4 nm), and inadequate electrical conductivity, constrain the photocatalytic efficiency of Fe_2O_3, leading to diminished quantum optical efficiency.[14] By combining with a second semiconductor, we can overcome these constraints and create a novel heterogeneous junction catalyst that offers exceptional benefits.[18–23] $ZnBi_2O_4$, a bismuthate compound, is considered a promising candidate owing to its exceptional characteristics. $ZnBi_2O_4$ is a well-established p-type semiconductor with a direct bandgap ranging from 2.2 to 3.0 eV,[24,25] which makes it highly appropriate for applications that utilize visible light or sun sources. $ZnBi_2O_4$ has a distinctive crystal structure, characterized by zigzag chains of metal–oxygen bonds formed by Zn and Bi atoms at the corners.[26] Moreover, $ZnBi_2O_4$ demonstrates chemical stability, a high optical current density, and the ability to undergo oxidation by hydroxyl ($^{\bullet}OH$) ions.[27,28]

Fe_2O_3 and $ZnBi_2O_4$ combinations can form n–p heterojunction semiconductors that are photocatalyst-driven under visible light or sun sources. Fe_2O_3 is an n-type semiconductor with the Fermi level located near the E_{CB}, whereas $ZnBi_2O_4$ is a p-type semiconductor with the Fermi level located near the E_{VB}. At the junction between the two semiconductors, electrons are transferred from Fe_2O_3 to $ZnBi_2O_4$ until their Fermi levels align, creating an electric field that can boost the transport and separation of photogenerated charges over $ZnBi_2O_4$.

In this study, a novel 3D Fe_2O_3@$ZnBi_2O_4$ n–p heterojunction was fabricated in two steps. Initially, the gel–polymer combustion technique produced Fe_2O_3 using tartaric acid and polyvinyl alcohol as the combustion agents. Next, $ZnBi_2O_4$ was introduced onto the Fe_2O_3 surface *via* microwave-assisted precipitation. In addition, the physicochemical properties and photocatalytic activities of the heterojunctions were studied and discussed in detail. Furthermore, the physicochemical characteristics and photocatalytic activity of the heterojunctions were comprehensively examined and analyzed. Additionally, experimental investigations into the function of oxidizing agents in the breakdown of MB have been conducted. A reaction mechanism for dye degradation was proposed.

2. Experimental

2.1 Materials

$Bi(NO_3)_3 \cdot 5H_2O$, $Zn(NO_3)_2 \cdot 6H_2O$, $Fe(NO_3)_3 \cdot 9H_2O$, NH_4OH, H_2O_2, $Na_2S_2O_8$, and methylene blue (MB) were purchased from Xilong Scientific Co. Tartaric acid, polyvinyl alcohol (PVA, $M = 145\,000$ g mol^{-1}, 99%), $AgNO_3$ (99.9%), disodium ethylenediamine tetraacetate (Na_2EDTA, 99%), isopropanol (Isp, 99.5%), phenol (Phe(OH), 99%), and 1,4-benzoquinone (*p*-BQ, 98%) were purchased from Sigma-Aldrich. All the reagents were used without further purification.

2.2 Synthesis of Fe_2O_3 materials

Synthesis of the Fe_2O_3 material was done using the combustion technique. 1.32 grams of PVA and tartaric acid (4.5 g) were combined in 80 mL of deionized water at 50 °C using a magnetic stirrer. The 0.5 M $Fe(NO_3)_3$ solution was added to the mixture slowly, 40 mL at a time, and the mixture was stirred well. Subsequently, the pH of the solution was modified to 4 using a 2 M NH_4OH solution. The reaction mixture was continuously agitated at 80 °C until water evaporated and transformed into a gelatinous substance. The gel was allowed to remain undisturbed overnight for aging and subsequently dried at 100 °C for 2 h. Finally, the gel was calcined at 500 °C for 2 h, leading to the formation of a brick-red powder containing Fe_2O_3.

2.3 Synthesis of Fe_2O_3@$ZnBi_2O_4$ materials

n–p Fe_2O_3@$ZnBi_2O_4$ was produced using a microwave-assisted precipitation method. The sample had a molar ratio of 2 : 1 between Fe_2O_3 and $ZnBi_2O_4$. The solution was prepared by dissolving 1.455 g of $Bi(NO_3)_3 \cdot 5H_2O$ in a 5% HNO_3 solution. Subsequently, 50 mL of 0.03 M $Zn(NO_3)_2$ solution was added, and the mixture was stirred using a magnetic stirrer for 30 minutes. In parallel, 0.48 g of previously synthesized Fe_2O_3 was dispersed in 100 mL of sonicated deionized water. This suspension was then introduced into the Bi–Zn solution and stirred for an additional 45 minutes. The pH of the resulting mixture was adjusted to 10 by the dropwise addition of a 2 M NH_4OH solution under continuous stirring. After stirring for 30 minutes, the reaction mixture was transferred to a 500 mL flask and subjected to microwave heating at 400 W for 45 min. The temperature of the reaction mixture was lowered to match the surrounding temperature; it was separated by filtering, and the resultant solid was cleaned by rinsing it with deionized water until it achieved a pH of 7. Finally, the mixture was subjected to a temperature of 500 °C for 3 h, followed by drying at 90 °C for 3 h, which resulted in the production of Fe_2O_3@$ZnBi_2O_4$ (FZB21). For comparative analysis, materials having Fe_2O_3/$ZnBi_2O_4$ molar ratios of 1 : 2 and 1 : 1 were produced and labeled as FZB12 and FZB11, respectively. The $ZnBi_2O_4$ sample synthesized under similar conditions, in the absence of Fe_2O_3, is denoted as ZBO.

2.4 Characterization

The composites were analyzed using X-ray diffraction (XRD) on a Bruker D8 Advance instrument (Germany) to investigate their phase compositions and crystal structures. The interfacial bonding characteristics of the material were analyzed using Fourier transform infrared spectroscopy (FTIR) with a PerkinElmer Spectrum Two instrument (United States). The optical absorption and bandgap properties of the material were analyzed by ultraviolet-visible diffuse reflectance spectroscopy (UV-Vis DRS) using a Jasco V670 (Japan), and photoluminescence (PL) measurements were conducted using a machine 205 Horiba iHR550 (Japan). The surface morphology and structure of materials were analyzed using a Hitachi S-4800 scanning electron microscope (SEM) from Japan and high-resolution transmission electron microscopy (HR-TEM) with an S-4800 NIHE model. The oxidation status of the elements in each catalyst was evaluated using X-ray photoelectron spectroscopy (XPS) with an ESCA-3400 apparatus (Shimadzu). The analysis was conducted using Mg Kα 175 radiation (1253.6 eV, 10 kV, 20 mA). Mott–Schottky plots, photocurrent curves, and Nyquist plots were obtained using a CHI 650E electrochemical workstation with a three-electrode cell in a 0.1 M Na_2SO_4 electrolyte solution.

2.5 Evaluating photocatalytic performance

The catalytic activity of the FZB powder was assessed by detecting the degradation of the MB dye under exposure to halogen light (150 W, Osram, Germany). The reaction consists of two steps.

To establish equilibrium between the adsorption and desorption of MB on the surface of the catalyst, the reaction mixture was stirred in the absence of light for 1 h as a step in the adsorption process.

Once the catalyst surface reaches the point of MB adsorption–desorption equilibrium, the breakdown process can be initiated by exposing it to light irradiation. To carry out the photocatalytic reaction, the light source was activated until most of the color was eliminated from the MB solution. A magnetic stirrer and circulating water were used to agitate the reaction mixture until it reached a steady state at ambient temperature. The catalyst was separated from the suspension by subjecting 3 mL of the mixture to centrifugation every 20 min. The MB concentration was determined using an ultraviolet-visible spectrophotometer.

3. Results

3.1 Charaterization of the 3D Fe_2O_3@$ZnBi_2O_4$ n–p (FZB) heterojunction

Fig. 1 displays the XRD patterns, which show the structure and crystalline phase composition of n–p FZB. The two crystalline phases constituting the FZB materials were α-Fe_2O_3 and $ZnBi_2O_4$. The lattice planes (012), (104), (110), (113), (024), (116), (214), and (300) exhibit the α-Fe_2O_3 phase, according to JCPDS card No. 79-0007.[29,30] The $ZnBi_2O_4$ (ZBO) tetragonal phase is clearly indicated by the diffraction peaks corresponding to the

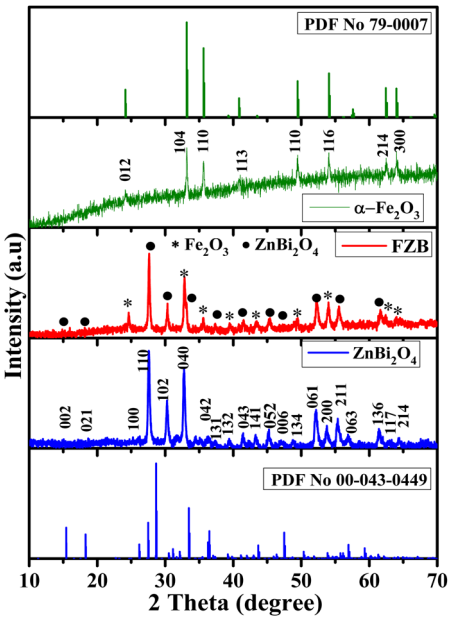

Fig. 1 XRD patterns of α-Fe_2O_3, ZBO, and FZB.

lattice planes (100), (201), (002), (211), (210), (301), (311), (212), (321), (322), (203), (421), (402), and (331). This matches the information in JCPDS card No. 00-043-0449.[31] These results indicated the successful synthesis of FZB heterostructures with good crystallinity.

Furthermore, SEM and TEM analysis were used to study the morphology and structure of the samples. The SEM image in Fig. 2A shows that the Fe_2O_3 material produced using the polymer gel combustion technique possessed a three-dimensional structure characterized by flat branches. These branches are formed from the amalgamation of several tiny planar particles during gel combustion. Besides, the FZB material (Fig. 2B) exhibited a 3D structure composed of two components. This structure consisted of flower-like clusters composed of $ZnBi_2O_4$, which were accompanied by long slender blades that covered the surface of the Fe_2O_3 branches. The Fe_2O_3 flat branches were seen to undergo rounder and larger size transformation after being subjected to microwave heating and calcination during the synthesis of FZB. In addition, the high-resolution TEM (HR-TEM) results confirmed the formation of an FZB heterojunction. The lattice fringes were approximately ~0.370 nm which is ascribed to the (012) plane of α-Fe_2O_3,[32,33] in which ~0.292 nm belongs to the (102) plane of $ZnBi_2O_4$. Together with the XRD findings mentioned earlier, this provides evidence that the FZB material was effectively synthesized using a two-step process.

Moreover, EDS spectra and elemental mapping of FZB further confirmed the effective synthesis of FZB. Fig. 2E–J illustrate that the sample contained Zn, Fe, Bi, and O and exhibited a very regular distribution. No extraneous foreign components were identified in any of the samples.

The chemical bonds of the catalysts were studied by FT-IR spectroscopy (Fig. 3). Fig. 3A shows that the absorption peaks at

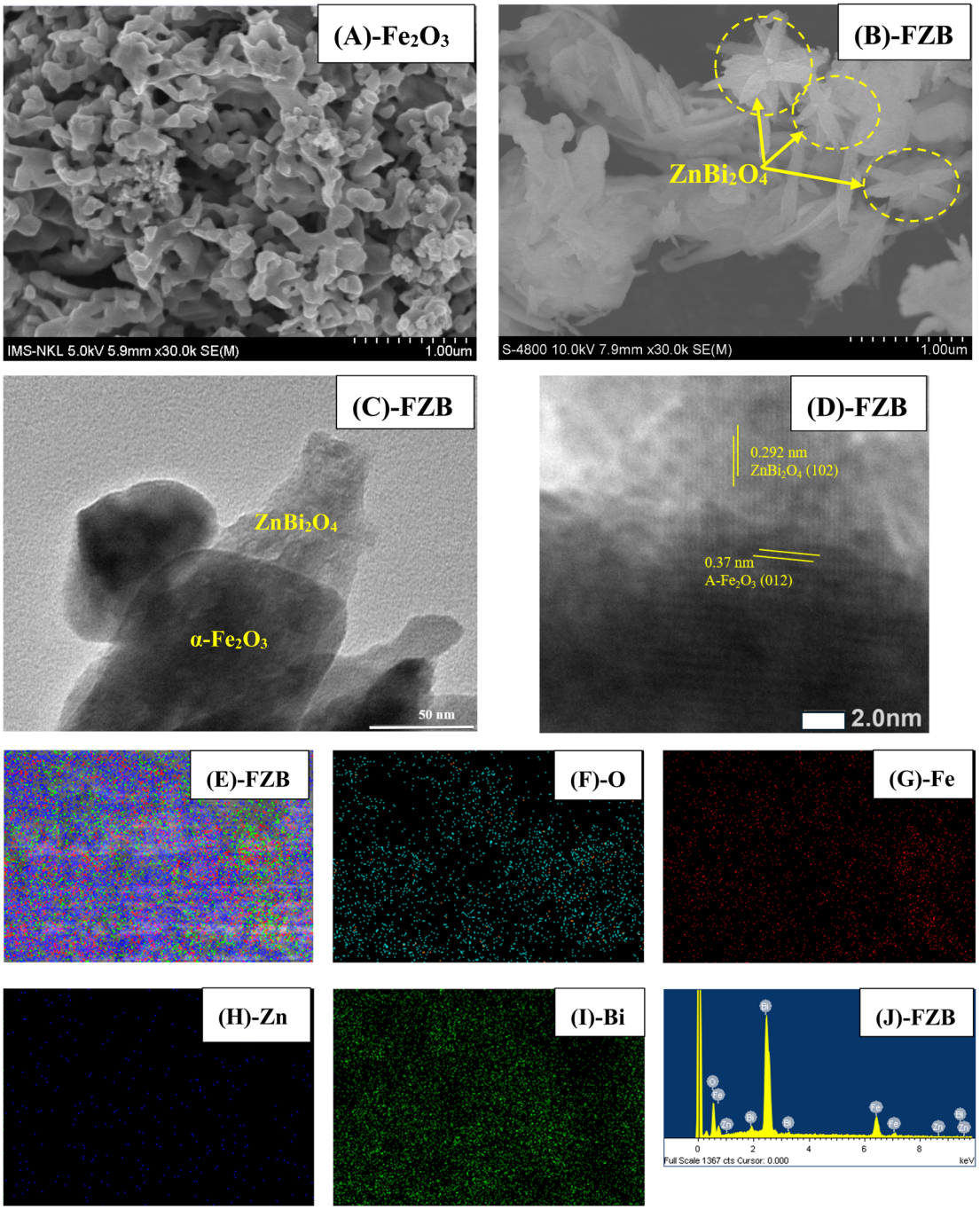

Fig. 2 SEM images of (A) Fe_2O_3 and (B) FZB; (C) TEM, (D) HR-TEM images of FZB, (E–I) EDS mapping of FZB, and (J) EDS spectra of FZB.

approximately 462 and 555 cm^{-1} of the Fe_2O_3 material can be attributed to the stretching vibrations of Fe–O.[20,34] For $ZnBi_2O_4$, the absorption peaks at 845 and 1390 cm^{-1} correspond to the Bi–O and Bi–O–Bi vibrations, respectively. Additionally, the peaks at 480, 528, and 575 cm^{-1} indicate the vibration of Zn–O bonds.[25,26,31,35] It is worth mentioning that the absorption peaks in the FT-IR spectrum of the FZB material are very strong and show bond metal oxygens, such as Zn–O, Fe–O, Bi–O, and Bi–O–Bi. Additionally, vibration peaks were observed in the range of 3300–3500 cm^{-1} attributed to O–H from absorbed H_2O. The FT-IR results further support the successful synthesis of n–p FZB heterojunctions.

The UV-Vis-DRS spectrum is associated with the optical absorption range and bandgap energy of the material. Fig. 3B demonstrates that in the ultraviolet light spectrum, the synthetic materials exhibited excellent absorption capabilities, with the order of absorption being ZBO < FZB < Fe_2O_3. In the visible light spectrum, the FZB and Fe_2O_3 materials exhibited significant absorption, whereas the ZBO material exhibited significantly weaker absorption. The optical absorption

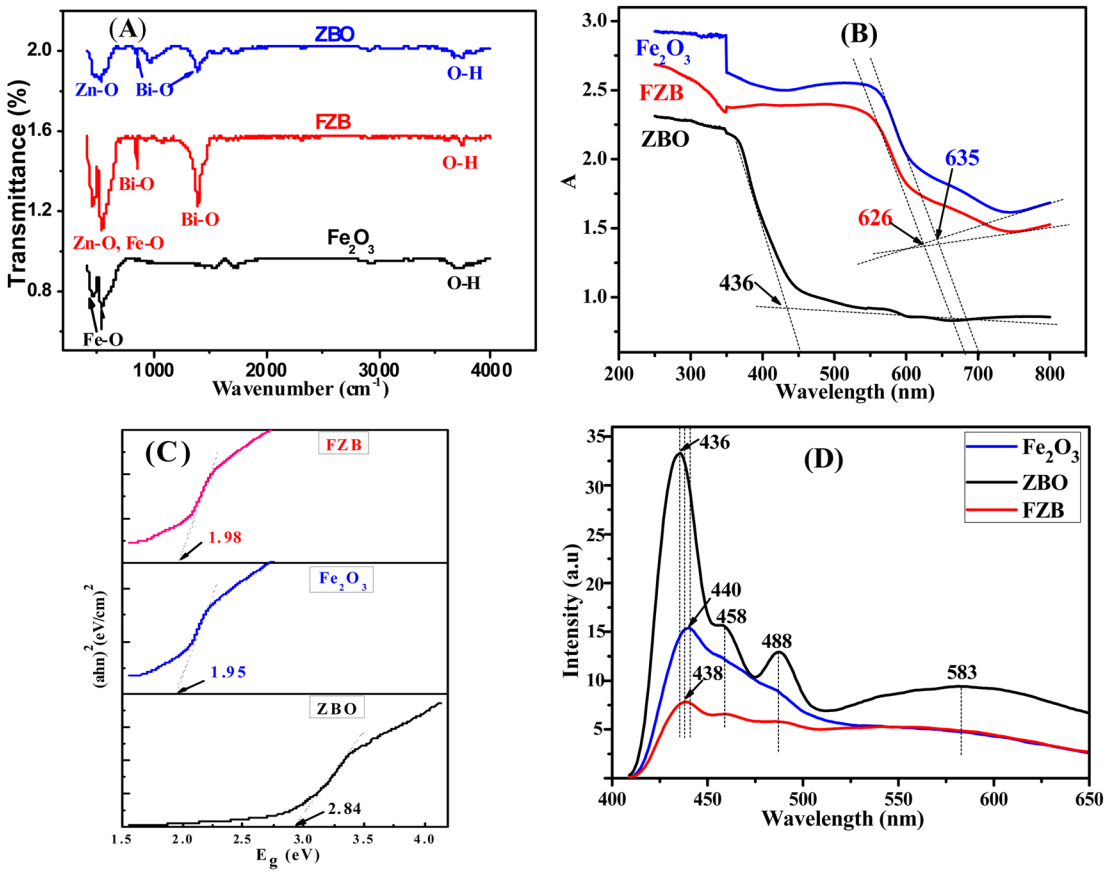

Fig. 3 (A) FTIR, (B) UV-Vis-DRS, (C) Tauc plots, and (D) PL spectra of Fe_2O_3, ZBO, and FZB.

characteristics can be verified by estimating the position of the optical absorption edge and bandgap of the material using the Tauc diagram (Fig. 3B and C).[36,37] The bandgaps of ZBO, Fe_2O_3, and FZB were measured at 2.84, 1.95, and 1.98 eV, respectively. The absorption wavelength of each material was determined using the formula $\lambda = hc/E_g$, resulting in values of 436, 635 nm for Fe_2O_3, and 626 nm for FZB. Thus, it can be deduced that ZBO exhibits a high capacity for absorbing ultraviolet rays and only partially absorbs visible light with a wavelength $\lambda \leq 436$ nm. However, both the FZB and Fe_2O_3 materials possess a strong ability to absorb light across the ultraviolet and visible regions of the light spectrum. The advantageous attribute of FZB is highly advantageous for the practical implementation of the FZB material as a solar photocatalyst, as it enables the utilization of sunlight as a light source to initiate the photocatalytic process. The new catalyst (FZB) has notable advantages in this regard.

In addition, the optical characteristics of the FZB material were studied using photoluminescence (PL) spectroscopy, which enables the investigation of both electron–hole recombination and charge separation in materials. The photoluminescence (PL) spectra of $ZnBi_2O_4$, Fe_2O_3, and FZB were recorded at an excitation wavelength of 400 nm. Fig. 3D shows that all emission peaks are situated exclusively within the visible light range, specifically in the deep-level emission (DLE) region. The strongest emission peak at 436 nm is related to the rapid recombination probability of electron–hole pairs in $ZnBi_2O_4$, and the peak position agrees well with the bandgap (2.84 eV) of $ZnBi_2O_4$. Meanwhile, the broad peak with the highest intensity at 440 nm was associated with the atomic transitions of iron vacancies in Fe_2O_3.[38] The weak shoulder peaks at 458 and 488 nm and a broad peak at 583 nm in the $ZnBi_2O_4$ PL spectra correspond to the $^3P_{0,1} \rightarrow {}^1S_0$ transitions of the Bi^{3+} ions.[39]

The formation of complexes on the heterogeneous surface reduced the PL intensity and peak position shift. The peak observed at 438 nm for the FZB composite exhibited a sharp decrease in intensity, and there was a slight red shift compared to that of pristine $ZnBi_2O_4$ (436 nm) and a slight blue shift compared to that of pure Fe_2O_3 (440 nm). The significant decrease in intensity indicates that after the formation of the heterojunction between Fe_2O_3 and $ZnBi_2O_4$, the rapid recombination of photogenerated free radicals was significantly inhibited. The broad monotonically shifted emission peak of the FZB nanocomposite was attributed to the presence of defect sites, leading to the generation of localized energy levels in the forbidden energy gap.

The surface chemistry of the synthesized $ZnBi_2O_4$ and FZB was analyzed using XPS. Fig. 4 shows the binding energies of the Zn 2p, O 1s, Fe 2p, and Bi 4f orbitals.

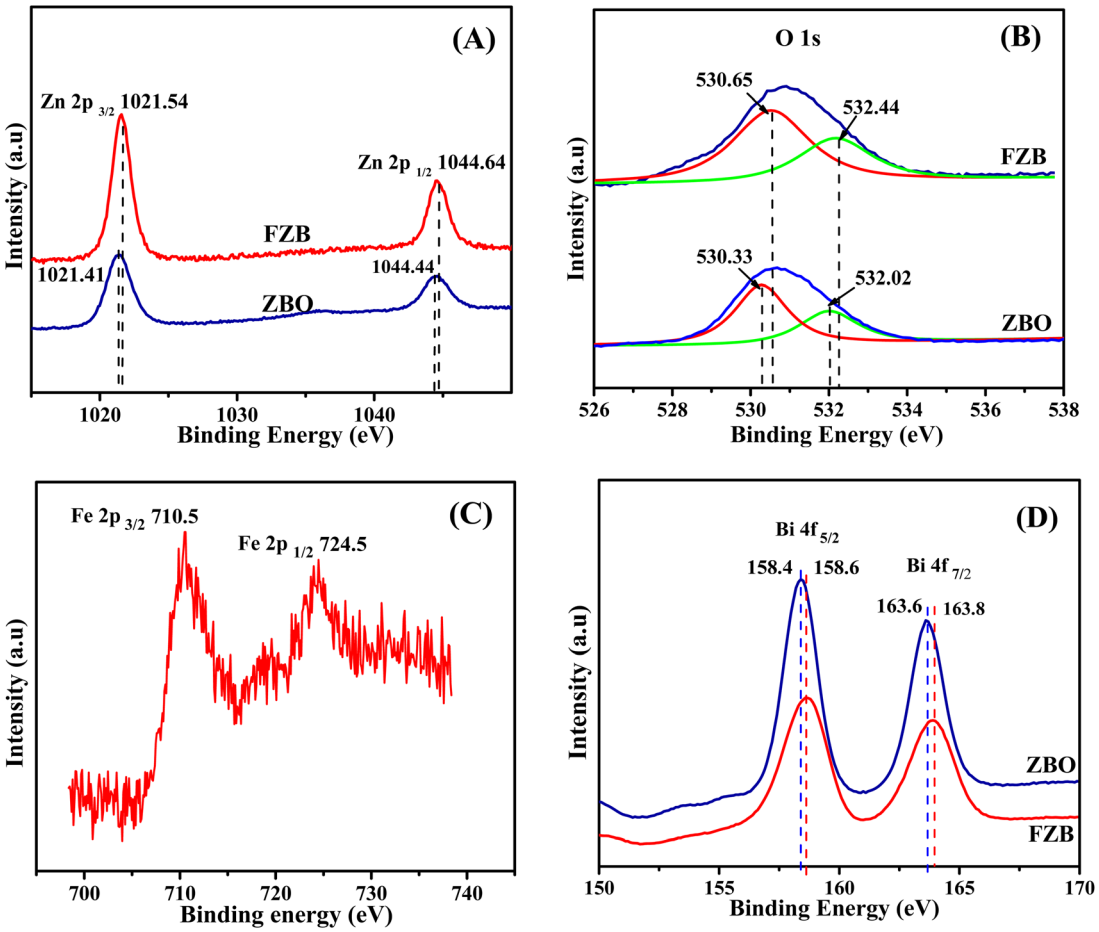

Fig. 4 XPS spectra of (A) FZB heterojunction and high-resolution (B) O 1s, (C) Fe 2p, and (D) Bi 4f XPS spectra.

The Zn 2p orbitals (Fig. 4A) of the FZB sample exhibit a complex electronic structure, as evidenced by the presence of two distinct peaks in the X-ray photoelectron spectroscopy (XPS) analysis. The peaks observed at 1021.54 eV and 1044.64 eV correspond to the energy levels of Zn $2p_{3/2}$ and Zn $2p_{1/2}$,[40] respectively. These energy levels are characteristic of spin–orbit splitting in the Zn2p orbitals, providing valuable information about the electronic configuration of zinc atoms within the composite material. The slight redshift observed in the binding energy peaks of the FZB sample compared to those of $ZnBi_2O_4$ (ZBO) is a significant indicator of the successful formation of the composite material. This shift in the binding energies suggests a change in the chemical environment surrounding the zinc atoms, likely due to the interaction between the Fe_2O_3 and $ZnBi_2O_4$ components.[41] The redshift may be attributed to factors such as charge transfer, changes in coordination, or alterations in the local electronic structure resulting from the integration of iron oxide into the zinc–bismuth oxide matrix.

The XPS spectrum of O 1s, as depicted in Fig. 4B, reveals two distinct peaks that provide valuable information regarding the oxygen species present in ZBO. The lattice oxygen (O^{2-}) at 530.33 eV represents the oxygen ions incorporated into the crystal lattice structure of the material. The surface-adsorbed oxygen (O^{-}) at 532.02 eV corresponds to the oxygen species absorbed on the surface of the material.[42] The XPS analysis of the FZB sample revealed a notable shift in the two peaks towards higher energy levels, indicating significant changes in the electronic structure of the material. The most striking difference is observed in the relative intensity of the 532.65 eV peak, which is markedly higher in FZB than in ZBO. This increase in the peak intensity is a strong indicator of a higher concentration of oxygen vacancies within the FZB sample. Oxygen vacancies play a crucial role in the electronic and optical properties of metal oxides and often serve as active sites for various chemical reactions.

Fig. 4C shows two prominent peaks of the Fe 2p core level at 710.7 eV, and 724.4 eV attributed to Fe $2p_{3/2}$ and Fe $2p_{1/2}$ states.[43,44] The reported binding energy values are consistent with the typical values for iron oxides, suggesting that the iron in the sample is likely to be in an oxidized state.

Fig. 4D shows that the two distinct peaks of 158.4 and 163.6 eV are related to the Bi $4f_{7/2}$ and Bi $4f_{5/2}$ spin-orbital pairs of Bi^{3+}, for $ZnBi_2O_4$.[45] The binding energies of Bi $4f_{7/2}$ (158.6 eV) and Bi $4f_{5/2}$ (163.8 eV) shifted to higher binding energies for FZB. This shift in binding energies suggests a change in the chemical environment of bismuth atoms when $ZnBi_2O_4$ is combined with Fe_2O_3.[46] The lower binding energies observed in FZB may indicate a reduction in the oxidation state of Bi or alterations in its electronic structure.

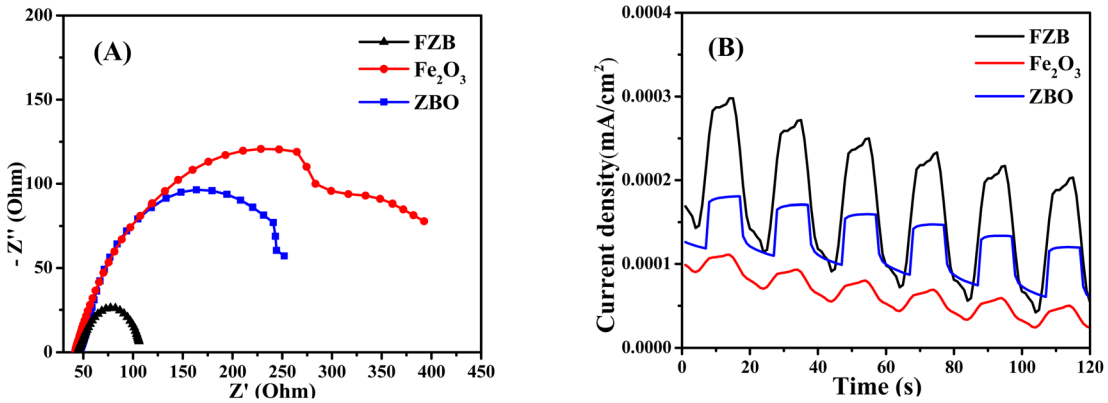

Fig. 5 (A) EIS curves and (B) transient photocurrent responses of Fe_2O_3, ZBO, and FZB.

Electrochemical impedance spectroscopy (EIS) and transient photocurrent measurements were performed to investigate the charge-transfer behavior. As illustrated in Fig. 5A, the Nyquist plot reveals that the arc radius of the two-component nanocomposite was smaller than that of the individual components. This indicates that the FZB heterostructure encounters fewer obstacles in the charge transfer across the interface, resulting in a higher charge separation efficiency. The reduced charge transfer resistance in the FZB heterostructure can be attributed to the synergistic effect between the two components, which facilitates electron–hole pair separation and enhances overall photocatalytic performance. This improvement in charge transfer dynamics is further supported by transient photocurrent measurements, which show a higher and more stable photocurrent response for the nanocomposite compared to the individual components. To validate these findings, the photocurrent responses of the samples were recorded over four on/off cycles (Fig. 5B). FZB exhibited significantly higher photocurrent responses than the Fe_2O_3 and $ZnBi_2O_4$ photocatalysts. These results confirm that the internal electric field generated at the n–p heterojunction interface between ZnO and $ZnBi_2O_4$ enhances charge separation and transport efficiency, consistent with the EIS and PL measurement results.

3.2 Photocatalytic activity of FZB

The photocatalytic activity was assessed by measuring the degradation efficiency of MB under visible-light irradiation. The experimental variables influencing photocatalytic activity, including the molar ratio of $Fe_2O_3/ZnBi_2O_4$, solution pH, and catalyst concentration, were investigated. The results are shown in Fig. 6. Experimental investigations were conducted to examine the impact of the molar ratio of $Fe_2O_3/ZnBi_2O_4$ on the pH of natural solutions. The data presented in Fig. 6A demonstrate that the heterojunctions were better than the pure components in the decolorization of MB. The MB degradation efficiency after 160 min of irradiation was 69.2% for Fe_2O_3 and 83.3% for ZBO. The degradation efficiencies of FZB12, FZB11, and FZB21 were 96.5, 98.1, and 99.5%, respectively. Furthermore, the Langmuir–Hinshelwood pseudo-first-order kinetic model was employed to compute the rate constant of the photocatalytic reaction. As shown in Fig. 6B, the reaction rate constant (k_{app}) for FZB21 is 0.0326 min^{-1}, which is higher than those of FZB12 (0.0213 min^{-1}) and FZB11 (0.0262 min^{-1}) and specifically surpasses those of Fe_2O_3 (0.0078 min^{-1}) by approximately 4.2 times and $ZnBi_2O_4$ (ZBO) (0.0116 min^{-1}) by 2.8 times. The improved effectiveness of decolorization is ascribed to the synergistic effect between ZBO and Fe_2O_3 in the heterojunction structure, which successfully limits the recombination of the photoexcited charge carriers.

The efficacy of photodegradation is frequently affected by the solution pH, partly because of its association with the surface charge of the catalyst, which subsequently affects the adsorption of organic compounds onto the catalyst surface. In this experiment, the pH of the solution was calibrated within an interval of 4–10. Fig. 6C and D illustrate that the decolorization of MB by FZB21 was slow at solution pH values ranging from 4 to 7; however, its rate greatly increased at solution pH values ranging from 8 to 10. After 45 min of exposure to light, the reaction rate constants varied between 0.017 min^{-1} and 0.020 min^{-1} within the pH range of 4–7. Within the pH range of 8–10, the values varied from 0.0572 to 0.0853 min^{-1}. The breakdown of MB was observed to be especially slow at pH values below 7, mostly because of the positive charge present on both the catalyst surface (pH_z of FZB21 = 7.8) and MB^+ ions. Thus, only a restricted amount of MB was absorbed onto the catalyst surface and underwent breakdown. At pH values greater than 7, the FZB21 surface had a negative charge, which facilitated the effective adsorption of MB onto its surface. Hence, the rate constant of the reaction increases and attains its maximum value at pH 10. Nevertheless, because of the highly alkaline pH of 10, this study employed a pH of 9.

Experimental investigations of the impact of the initial concentration of the MB solution on the effectiveness of MB decolorization are shown in Fig. 6E and F. The results indicated that the decline in the MB concentration exhibited a progressive reduction as the initial MB concentration increased from 30 to 60 ppm. At a concentration of 30 ppm, MB exhibited a reaction rate constant of 0.0698 min^{-1}, 40 ppm at 0.0536 min^{-1}, 50 ppm at 0.0294 min^{-1}, and 60 ppm at 0.0206 min^{-1}. The reduction in efficiency with an increasing initial MB concentration is attributed to the light-blocking phenomenon. The deeper hue of the solution obstructs the ability of the catalyst to absorb

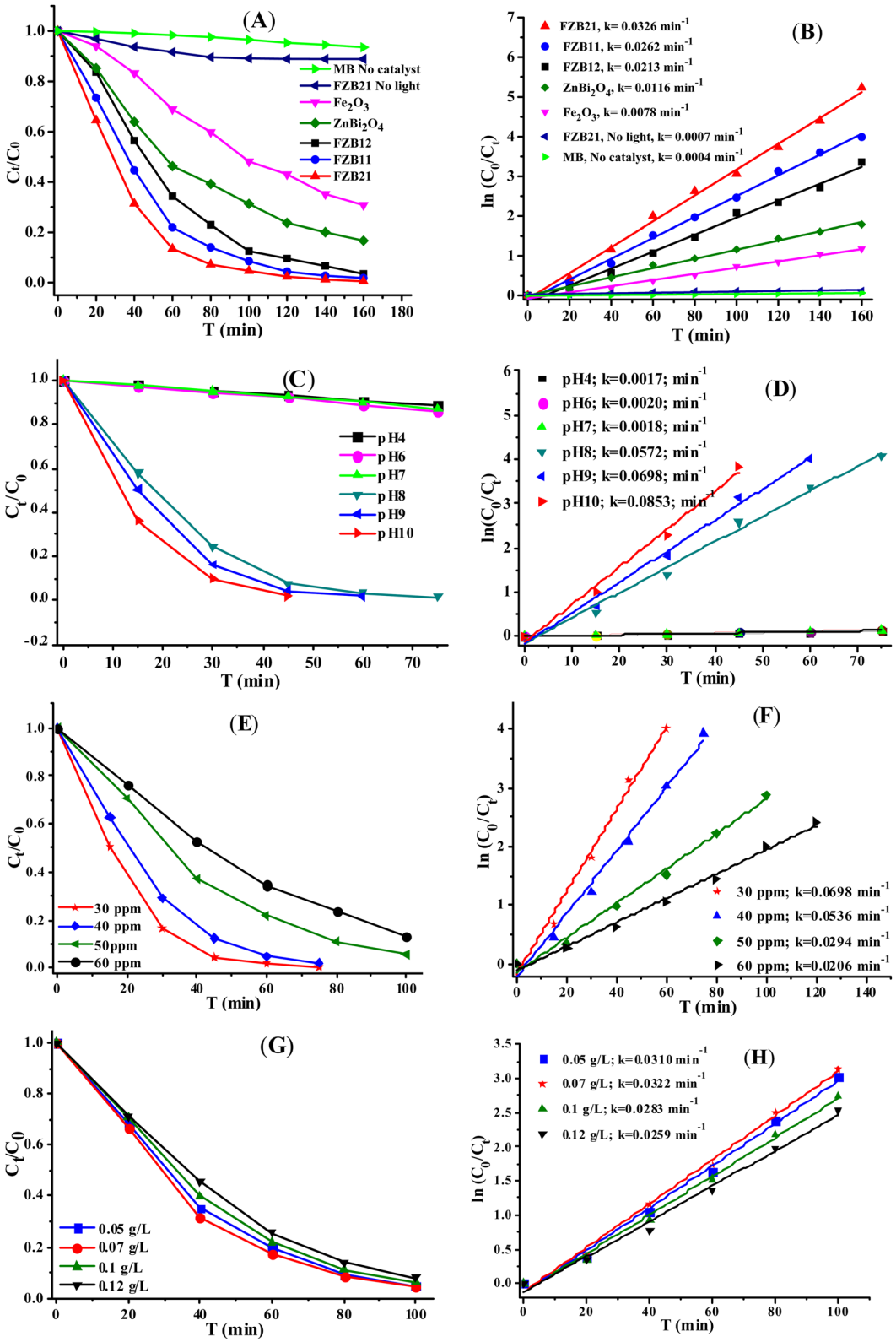

Fig. 6 Effects of the molar ratio of $Fe_2O_3/ZnBi_2O_4$ (A)–(B), solution pH (C) and (D), initial MB concentration (E) and (F), and photocatalyst concentration (G) and (H) on MB degradation using the FZB heterojunction under visible light.

light, resulting in a reduction in the concentration of photoexcitation charge carriers, which is the process responsible for organic matter biodegradation.

Furthermore, the effect of the catalyst concentration was also investigated. Fig. 6G and H indicate that the efficiency of MB degradation approached 0.0310 min^{-1} when the catalyst

concentration was 0.5 g L^{-1} and significantly increased to 0.0322 min^{-1} when the catalyst concentration was 0.7 g L^{-1}. Nevertheless, the efficiency of MB degradation declined to 0.0283 and 0.0259 when the catalyst concentration was raised to 1.0 and 1.2 g L^{-1}, respectively. The reduction in efficiency can be attributed to two factors: first, the surplus catalyst induces a light-blocking phenomenon, and second, it facilitates competition for the active sites on the catalyst surface.

To study the parameters influencing the efficiency of MB degradation, the optimal conditions for the photocatalytic reaction were determined as follows: FZB21 material, pH 9, MB concentration 60 ppm, catalyst content 0.7 g L^{-1}.

Additionally, we performed a series of studies to evaluate the influence of H_2O_2 and $K_2S_2O_8$ on the MB degradation efficiency under optimal conditions. Fig. 7A and B indicate that in the absence of light, the degradation of MB was significantly challenging in the presence of a catalyst and H_2O_2, yielding a rate constant of $k = 0.00173$ min^{-1} and a degradation efficiency of only 13.9%. In contrast, exposure to light resulted in a substantial reduction in the MB concentration. The reaction rate constants were $k = 0.0322$ min^{-1} for 0 mM H_2O_2, $k = 0.0338$ min^{-1} for 2 mM H_2O_2, $k = 0.0645$ min^{-1} for 4 mM H_2O_2, and $k = 0.0695$ min^{-1} for 8 mM H_2O_2. The addition of H_2O_2 increased the reaction rate by a factor of 2.0 with 4 mM H_2O_2 and by a factor of 2.15 with 8 mM H_2O_2. Doubling the concentration of H_2O_2 from 4 to 8 mM resulted in a small increase in the reaction rate constant, indicating that the 4 mM concentration of H_2O_2 was nearly optimal. The introduction of H_2O_2 initiated the photo-Fenton reaction (H_2O_2/Vis, Fe_2O_3/H_2O_2), augmenting the concentration of $^{\cdot}OH$ and $^{\cdot}HO_2$ in the solution (reactions (1)–(3)). This facilitated the expedited breakdown of MB[47–49]

$$Fe^{3+} + e^- \rightarrow Fe^{2+} \quad (1)$$

$$Fe^{2+} + H_2O_2 \rightarrow Fe^{3+} + {}^{\cdot}HO + OH^- \quad (2)$$

$$Fe^{3+} + H_2O_2 \rightarrow H^+ + Fe^{2+} + {}^{\cdot}HO_2{}^- \quad (3)$$

Furthermore, the effect of $S_2O_8{}^{2-}$ ions on the photodegradation efficiency of FZB was also studied (Fig. 7C and D). The reaction rate constant augmented by 1.5 times ($k = 0.0486$ min^{-1}) for 1 mM $K_2S_2O_8$, 5.7 times ($k = 0.1836$ min^{-1}) for 2.0 mM $K_2S_2O_8$, and 5.95 times ($k = 0.1917$ min^{-1}) for 3 mM $K_2S_2O_8$. Electrons generated using light interact with $Na_2S_2O_8$ on the surface of the catalyst to create ROS radicals $^{\cdot}SO_4{}^-$ and $^{\cdot}OH$ (reactions (1), (4)–(7))[50,51] which accelerates the reaction. The reaction slows the recombination of photogenerated electrons and holes, and $K_2S_2O_8$, acts as an electron trapping agent. At the same time, it creates reactive oxygen species (ROS), which make the strong oxidizing agent more effective at breaking down methylene blue (MB).

$$Fe^{3+} + S_2O_8{}^{2-} \rightarrow {}^{\cdot}S_2O_8{}^{2-} + Fe^{2+} \quad (4)$$

$$S_2O_8{}^{2-} + Fe^{2+} \rightarrow {}^{\cdot}SO_4{}^- + SO_4{}^{2-} + Fe^{3+} \quad (5)$$

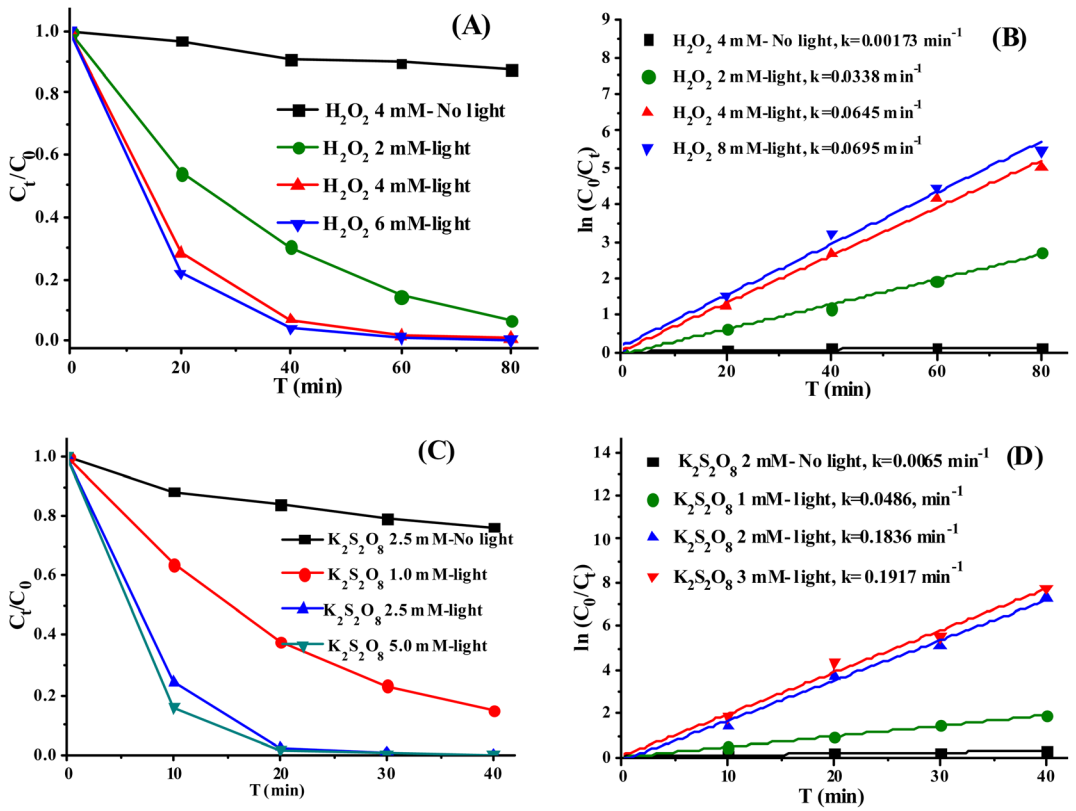

Fig. 7 Effect of H_2O_2 (A) and (B) and $K_2S_2O_8$ (C) and (D) on MB degradation using the FZB heterojunction under visible light.

$$S_2O_8^{2-} + e^- \rightarrow {}^{\cdot}SO_4^- + SO_4^{2-} \quad (6)$$

$${}^{\cdot}SO_4^- + H_2O \rightarrow {}^{\cdot}HO + SO_4^{2-} + H^+ \quad (7)$$

The use of $K_2S_2O_8$ significantly improved the effectiveness of MB degradation relative to that of H_2O_2. After 80 minutes of irradiation, the MB decomposition efficiency of FZB/H_2O_2 exceeded 99.4%, but the MB decomposition efficiency of FZB/$K_2S_2O_8$ attained 99.9% after merely 40 minutes of irradiation. The reaction rate constant for FZB/$K_2S_2O_8$ was 0.1917 min^{-1}, which is 2.8 times greater than that of FZB/H_2O_2 at 0.695 min^{-1}. There are several reasons why the MB decomposition reaction with $K_2S_2O_8$ was much faster than that with H_2O_2. (i) The first is that the O–O bond energy in $K_2S_2O_8$ is lower than that in H_2O_2 (213.3 kJ mol^{-1}), which makes $S_2O_8^{2-}$ more reactive than O_2^{2-}.[52] (ii) The second step involves the addition of $K_2S_2O_8$, which generates radicals ${}^{\cdot}SO_4^-$, ${}^{\cdot}S_2O_8^{2-}$, and ${}^{\cdot}HO$ (reactions (1), (2) and (4)–(7)), while the addition of H_2O_2 produces ${}^{\cdot}HO$ and ${}^{\cdot}HO_2^-$ (reactions (1)–(3)). The standard reduction potential of ${}^{\cdot}SO_4^-$ (2.5–3.1 V) exceeds that of ${}^{\cdot}HO$ (1.7–2.7 V) and ${}^{\cdot}HO_2^-$ (1.8 V). At neutral pH, the ${}^{\cdot}SO_4^-$ radical has a higher standard oxidation potential than the hydroxyl radical. It can successfully interact with organic molecules across a wide pH range of 2–8. (iii) The third is the sulfate radical, which is more selective and effective than ${}^{\cdot}HO$ radicals and can transfer electrons to organic molecules with aromatic or unsaturated bonds.[53] (iv) Finally, the half-life of ${}^{\cdot}SO_4^-$ is 30–40 μs, exceeding that of ${}^{\cdot}HO$ at 1 μs, and it can oxidize contaminants at an exceptionally high rate of 106–109 M s^{-1}.[54,55] The prolonged half-life enhances substantial interactions and mass transfer between ${}^{\cdot}SO_4^-$ radical and reactants.

These results demonstrate that the FZB catalyst effectively degrades MB under visible light, demonstrating its superior photocatalytic capabilities. The incorporation of minor quantities of oxidants (hydrogen peroxide and sodium persulfate), especially persulfate, significantly improved this characteristic.

3.3 Proposed mechanism

Experiments with selective scavengers at 1 mM doses were conducted to investigate the involvement of the reaction species in the degradation of MB. Na_2EDTA sequestered h^+, *p*-BQ sequestered ${}^{\cdot}O_2^-$, Isp sequestered ${}^{\cdot}OH$, $AgNO_3$ sequestered e^-, and PheOH sequestered ${}^{\cdot}SO_4^-$.[56–60] Fig. 8A and B illustrate that the rate of MB breakdown diminished owing to the inhibitory effects of the scavengers. The use of *p*-BQ, Isp, $AgNO_3$, and Na_2EDTA resulted in MB degradation efficiencies of 87.8, 77.7, 56.9, and 48.9%, respectively. The efficiency of MB degradation decreased marginally with the introduction of *p*-BQ and Iso but declined significantly with the incorporation of $AgNO_3$ and EDTA. This indicates that ${}^{\cdot}O_2^-$, ${}^{\cdot}OH$, e^-, and h^+ oxidants collaboratively decompose MB by photocatalysis, with e^- and h^+ assuming the most significant roles. Moreover, the incorporation of persulfate and PheOH scavengers markedly lowered the degradation efficiency of MB by 33.3% and 68.4%, respectively, after 40 and 80 min of illumination, respectively, underscoring

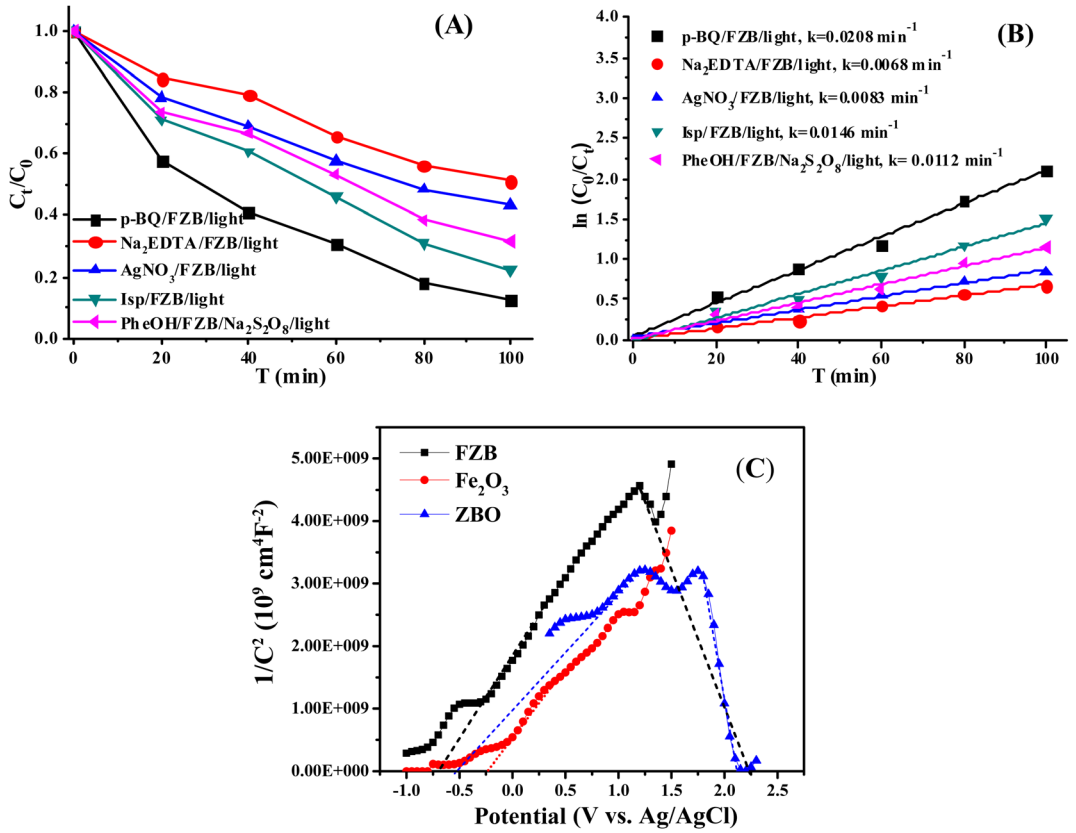

Fig. 8 Effect of radical scavengers (A and B) on MB degradation using FZB. (C) Mott–Schottky plots of Fe_2O_3, ZBO, and FZB.

the essential coordinating function of the $^{\bullet}SO_4$ radical in MB degradation.

Fig. 8C illustrates that the Mott–Schottky (M–S) plots exhibit a positive slope for n-type semiconductors and a negative slope for p-type semiconductors. The M–S plot of Fe_2O_3 exhibited a positive slope, signifying n-type semiconductor characteristics. The M–S curve of $ZnBi_2O_4$ has a negative slope, confirming its p-type characteristics. The flat band potentials of Fe_2O_3 and $ZnBi_2O_4$ were ascertained to be +0.28 V and +2.20 V *vs.* Ag/AgCl at pH 7 (corresponding to +0.485 V and +2.425 V *vs.* NHE), respectively. In n-type semiconductors, the conduction band (E_{CB}) is generally positioned 0.1 V above the flat potential, whereas in p-type semiconductors, the valence band (E_{VB}) is typically situated 0.1 V below the flat potential. The E_{CB} of Fe_2O_3 was established at +0.385 V, whereas the E_{VB} of $ZnBi_2O_4$ was computed to be +2.525 V.

The E_{VB} of Fe_2O_3 and the E_{CB} of $ZnBi_2O_4$ were computed using the formula $E_{VB} = E_{CB} + E_g$, where E_g represents the energy bandgap. The band gap values of Fe_2O_3 and $ZnBi_2O_4$ are 1.95 eV and 2.84 eV, respectively, with the E_{VB} of Fe_2O_3 estimated at +2.355 V and the E_{CB} of $ZnBi_2O_4$ estimated at −0.315 V. The photocatalytic mechanism for the Fe_2O_3@$ZnBi_2O_4$ nanocomposite is depicted in Fig. 9, based on these analytical and computational findings.

The introduction of p-type $ZnBi_2O_4$ onto the surface of n-type Fe_2O_3 resulted in the formation of an n–p heterojunction. This configuration induces fluctuations in the energy bands of $ZnBi_2O_4$ and Fe_2O_3 until achieving Fermi equilibrium. An internal electrostatic field is formed from Fe_2O_3 to $ZnBi_2O_4$, which facilitates charge separation. Upon exposure to visible light, $ZnBi_2O_4$ and Fe_2O_3 are stimulated to produce electron–hole pairs (e^-/h^+) (reaction (8)). The conduction band level of $ZnBi_2O_4$ was inferior to that of Fe_2O_3 following the formation of the n–p heterojunction. This indicates that the excited electrons of $ZnBi_2O_4$ can readily transition into the conduction band (CB) of Fe_2O_3. Conversely, the valence band (VB) level of Fe_2O_3 is more positive than that of $ZnBi_2O_4$, allowing the excited holes of Fe_2O_3 to transfer to the VB level of $ZnBi_2O_4$. The internal electric field at the interface between Fe_2O_3 and $ZnBi_2O_4$ propels these reactions. The internal electric field of the p–n heterojunction efficiently segregates the photogenerated charges.[61] This significantly reduced the recombination of e^-/h^+ pairs in the Fe_2O_3/$ZnBi_2O_4$ heterojunction. Photoluminescence studies, photocurrent response, electrochemical impedance spectroscopy, and radical scavenger investigations validated the capacity for charge separation.

Moreover, the electrons at the heightened conduction band level of $ZnBi_2O_4$ can reduce the adsorbed O_2 on the surface to form superoxide anion radicals ($^{\bullet}O_2^-$) (reaction (8)), while the holes at the lowered valence band level of Fe_2O_3 can oxidize the adsorbed H_2O on the surface to yield hydroxyl radicals ($^{\bullet}OH$) (reaction (9)). Owing to the abundance of electrons at the conduction band level in Fe_2O_3, Fe^{3+} can undergo oxidation to Fe^{2+} (reaction (11)), resulting in the formation of $^{\bullet}OH$ radicals (reaction (12)). The radicals exhibiting potent oxidizing characteristics, along with vacancies in the valence band of $ZnBi_2O_4$ and electrons in the conduction band of Fe_2O_3, contribute to the mineralization of the dye into CO_2, H_2O, and other inorganic byproducts (reaction (19)).

In the presence of H_2O_2, photo-Fenton processes occur, generating additional $^{\bullet}OH$ and $^{\bullet}HO_2^-$ radicals. This accelerated the reaction and enhanced its efficacy for the decomposition of

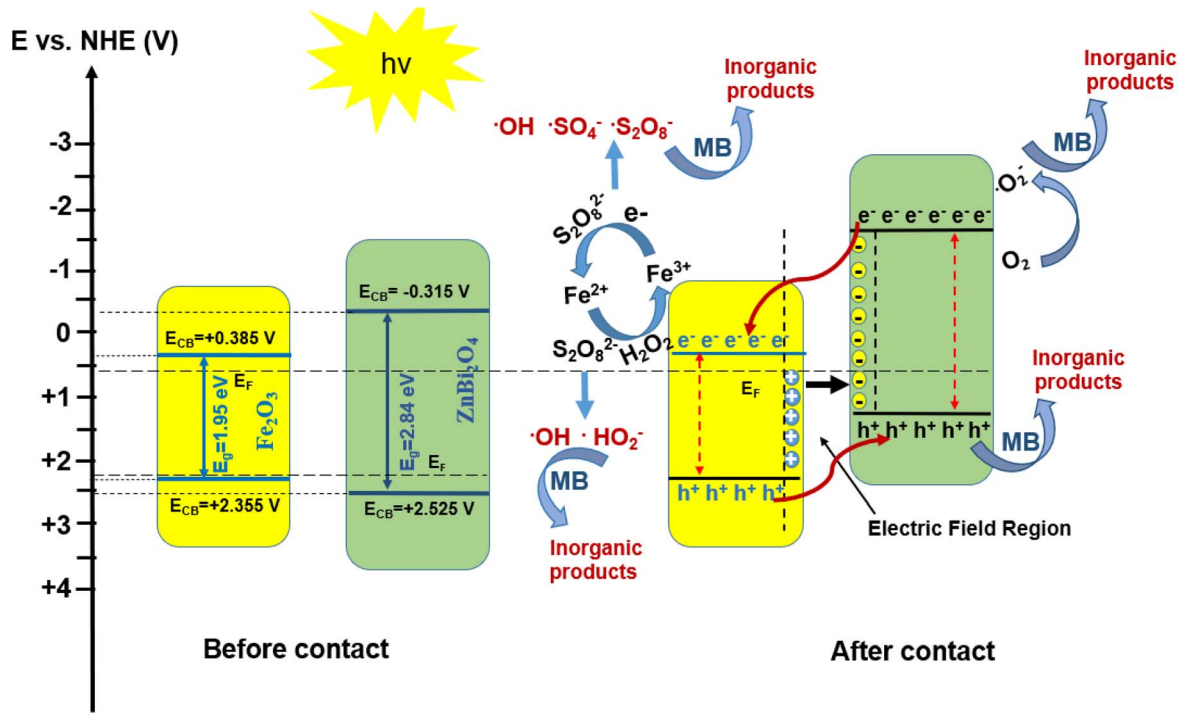

Fig. 9 Hypothesized mechanisms for MB degradation using the FZB catalyst under visible light.

MB. It was specifically the presence of $K_2S_2O_8$ that sped up the breakdown of MB by creating $^{\bullet}SO_4^-$ and $^{\bullet}S_2O_8^-$ radicals, which then increased the amount of $^{\bullet}OH$ (reactions (15)–(18)). It is known that the radicals $^{\bullet}SO_4^-$, $^{\bullet}S_2O_8^-$, and $^{\bullet}HO$ are all strong oxidizing agents. The $^{\bullet}SO_4^-$ radical strongly reacts with aromatic chemicals. The addition of persulfate significantly accelerated the MB breakdown reaction in the presence of the FZB catalyst and visible light (reaction (20)).

$$(\text{p–n})\text{FZB} + h\nu \rightarrow e^- + h^+ \quad (8)$$

$$e^- + O_2 \rightarrow {}^{\bullet}O_2^- \quad (9)$$

$$h^+ + H_2O \rightarrow {}^{\bullet}OH + H^+ \quad (10)$$

$$e^- + Fe^{3+} \rightarrow Fe^{2+} \quad (11)$$

$$Fe^{2+} + H_2O + e^- \rightarrow {}^{\bullet}OH + Fe^{3+} + H^+ \quad (12)$$

$$Fe^{2+} + H_2O_2 \rightarrow Fe^{3+} + {}^{\bullet}HO + OH^- \quad (13)$$

$$Fe^{3+} + H_2O_2 \rightarrow H^+ + Fe^{2+} + {}^{\bullet}HO_2^- \quad (14)$$

$$Fe^{3+} + S_2O_8^{2-} \rightarrow {}^{\bullet}S_2O_8^- + Fe^{2+} \quad (15)$$

$$S_2O_8^{2-} + Fe^{2+} \rightarrow {}^{\bullet}SO_4^- + SO_4^{2-} + Fe^{3+} \quad (16)$$

$$S_2O_8^{2-} + e^- \rightarrow {}^{\bullet}SO_4^- + SO_4^{2-} \quad (17)$$

$$^{\bullet}SO_4^- + H_2O \rightarrow {}^{\bullet}HO^- + SO_4^{2-} + H^+ \quad (18)$$

$$e^-, h^+, {}^{\bullet}OH, {}^{\bullet}O_2^- + \text{MB} \rightarrow CO_2 + H_2O + \text{inorganic products} \quad (19)$$

$$e^-, h^+, {}^{\bullet}OH, {}^{\bullet}O_2^-, {}^{\bullet}HO_2^- + \text{MB} \rightarrow CO_2 + H_2O + \text{inorganic products} \quad (20)$$

$$e^-, h^+, {}^{\bullet}OH, {}^{\bullet}O_2^-, {}^{\bullet}SO_4^-, {}^{\bullet}S_2O_8^- + \text{MB} \rightarrow CO_2 + H_2O + \text{inorganic products} \quad (21)$$

4. Conclusion

In conclusion, a novel 3D Fe_2O_3@$ZnBi_2O_4$ n–p heterojunction was successfully synthesized using two simple methods. The structural, morphological, optical, and electrochemical properties of the photocatalyst were examined. The photocatalytic activity of FZB under visible light was evaluated under various settings. With a molar ratio of 2/1 for Fe_2O_3 and $ZnBi_2O_4$, FZB had the most photocatalytic activity, 4.2 times that of Fe_2O_3 and 2.8 times that of $ZnBi_2O_4$. Over 95% of the 50 ppm MB solution broke down after 100 minutes of light exposure. This happened under the best conditions, with a $Fe_2O_3/ZnBi_2O_4$ molar ratio of 2 : 1, a pH of 9, and a catalyst concentration of 0.7 g L^{-1}. Furthermore, a photocatalytic reaction involving H_2O_2 and persulfate activation of FZB was conducted, resulting in rate constants that increased by 2.15 and 5.95, respectively. The small bandgap energy (E_g = 1.98 eV) of FZB makes it a better photocatalyst because it absorbs UV and visible light with $\lambda \leq$ 626 nm. The construction of the FZB n–p heterojunction efficiently segregates photogenerated charges, reducing their recombination rate, and the electric field in the heterojunction boosts the charge transfer. Moreover, the distinctive 3D architecture of FZB can produce a greater number of catalytically active sites. The investigation of the roles of reaction species and the energy band structures of the materials culminated in the proposal of a reaction mechanism.

Data availability

Data for this article, including origin data, are available at https://dx.doi.org/10.6084/m9.figshare.28458698.

Conflicts of interest

The authors declare that they have no competing financial interests or personal relationships that could influence the work reported in this study.

Acknowledgements

This work was supported by the Industrial University of Ho Chi Minh City (IUH), Ho Chi Minh, Vietnam, under grant number 50/HĐ-ĐHCN.

References

1 T. Robinson, G. McMullan, R. Marchant and P. Nigam, *Bioresour. Technol.*, 2001, **77**, 247–255.
2 J. J. Rueda-Marquez, I. Levchuk, P. Fernández Ibañez and M. Sillanpää, *J. Cleaner Prod.*, 2020, **258**, 120694.
3 G. Ren, H. Han, Y. Wang, S. Liu, J. Zhao, X. Meng and Z. Li, *Nanomaterials*, 2021, **11**, 1804.
4 N. Gaur, D. Dutta, A. Singh, R. Dubey and D. V. Kamboj, *Front. Environ. Sci.*, 2022, **10**, DOI: 10.3389/fenvs.2022.872514.
5 C. Karthikeyan, P. Arunachalam, K. Ramachandran, A. M. Al-Mayouf and S. Karuppuchamy, *J. Alloys Compd.*, 2020, **828**, 154281.
6 N. Alahmadi, *Separations*, 2022, **9**, 264.
7 M. A. Al-Nuaim, A. A. Alwasiti and Z. Y. Shnain, *Chem. Pap.*, 2023, **77**, 677–701.
8 Y. Chu, C. Zhao, Y. Zheng, X. Ren, S. Yuan, L. Zhao, Y. Wu and Y. He, *J. Environ. Sci.*, 2025, **154**, 444–456.
9 H. Baniamerian, M. Safavi, M. Alvarado-Morales, P. Tsapekos, I. Angelidaki and S. Shokrollahzadeh, *Environ. Res.*, 2018, **166**, 497–506.
10 D. C. Ashiegbu and H. J. Potgieter, *Heliyon*, 2023, **9**, e20674.
11 W. Wu, S. Zhang, X. Xiao, J. Zhou, F. Ren, L. Sun and C. Jiang, *ACS Appl. Mater. Interfaces*, 2012, **4**, 3602–3609.
12 M. Tahir and N. A. S. Amin, *Appl. Catal., B*, 2015, **162**, 98–109.
13 H. Kumari, S. Sonia, R. Ranga, S. Chahal, S. Devi, S. Sharma, S. Kumar, P. Kumar, S. Kumar, A. Kumar and R. Parmar, *Water, Air, Soil Pollut.*, 2023, **234**, 349.

14 M. Mishra and D. M. Chun, *Appl. Catal., A*, 2015, **498**, 126–141.
15 H. N. Luong, L. Ngoc, T. Nguyen, T. M. Dinh, N. Dan, N. Huynh, L. T. Duy, C. K. Tran and V. Q. Dang, *Sci. Technol. Dev. J.*, 2024, **27**, 3453–3462.
16 S. Lubis, Sheilatina and Murisna, *J. Phys.:Conf. Ser.*, 2018, **1116**, 042016.
17 C. N. C. Hitam and A. A. Jalil, *J. Environ. Manage.*, 2020, **258**, 110050.
18 F. Ge, X. Li, M. Wu, H. Ding and X. Li, *RSC Adv.*, 2022, **12**, 8300–8309.
19 T. Xie, Y. Liu, H. Wang and Z. Wu, *Sci. Rep.*, 2019, **9**, 1–12.
20 X. Zheng, M. Huang, Y. You, H. Peng and J. Wen, *Mater. Res. Bull.*, 2018, **101**, 20–28.
21 N. Mao, *Sci. Rep.*, 2019, **9**, 12383.
22 E. C. Pastrana, P. G. Ramos, L. A. Sánchez and J. M. Rodriguez, *Thin Films - Deposition Methods and Applications*, 2022, DOI: **10.5772/intechopen.105818**.
23 H. Baniamerian, M. Safavi, M. Alvarado-Morales, P. Tsapekos, I. Angelidaki and S. Shokrollahzadeh, *Environ. Res.*, 2018, **166**, 497–506.
24 A. Bahadoran, S. Masudy-Panah, J. R. De Lile, J. Li, J. J. Gu, B. Sadeghi, S. Ramakrishna and Q. Liu, *Int. J. Hydrogen Energy*, 2021, **46**, 24094–24106.
25 N. T. M. Tho, D. N. N. Khanh, N. Q. Thang, Y. I. Lee and N. T. K. Phuong, *Environ. Sci. Pollut. Res.*, 2020, **27**, 11127–11137.
26 R. Nithya and S. Ayyappan, *J. Photochem. Photobiol., A*, 2020, **398**, 112591.
27 A. Bahadoran, S. Masudy-Panah, J. R. De Lile, J. Li, J. J. Gu, B. Sadeghi, S. Ramakrishna and Q. Liu, *Int. J. Hydrogen Energy*, 2021, **46**, 24094–24106.
28 O. Baaloudj, A. A. Assadi, M. Azizi, H. Kenfoud, M. Trari, A. Amrane, A. A. Assadi and N. Nasrallah, *Appl. Sci.*, 2021, **11**(9), 3975.
29 M. Qayoom, K. A. Shah, A. H. Pandit, A. Firdous and G. N. Dar, *J. Electroceram.*, 2020, **45**, 7–14.
30 M. Hjiri, *J. Mater. Sci.: Mater. Electron.*, 2020, **31**, 5025–5031.
31 A. Habibi-Yangjeh, M. Pirhashemi and S. Ghosh, *J. Alloys Compd.*, 2020, **826**, 154229.
32 C. Wang, L. Wang and K. Tang, *Int. J. Electrochem. Sci.*, 2013, **8**, 4543–4550.
33 X. Liang, J. Qian, Y. Liu, Z. Zhang and D. Gao, *RSC Adv.*, 2020, **10**, 29077–29081.
34 S. Singh, G. Hitkari and G. Pandey, *Inorg. Nano-Met. Chem.*, 2018, **48**, 477–485.
35 V. A. Mane, D. V. Dake, N. D. Raskar, R. B. Sonpir, E. Stathatos and B. N. Dole, *Results Chem.*, 2023, **6**, 101083.
36 T. V. Ha Luu, N. N. Dao, H. A. Le Pham, Q. B. Nguyen, V. C. Nguyen and P. H. Dang, *RSC Adv.*, 2023, **13**, 5208–5218.
37 B. D. Viezbicke, S. Patel, B. E. Davis and D. P. Birnie, *Phys. Status Solidi B*, 2015, **252**, 1700–1710.
38 P. Thomas, *SB Academic Review*, 2016, **18**, 108–116.
39 A. M. Djaballah, R. Bagtache and M. Trari, *J. Mater. Sci.: Mater. Electron.*, 2022, **33**, 18410–18419.
40 A. Habibi-Yangjeh, M. Pirhashemi and S. Ghosh, *J. Alloys Compd.*, 2020, **826**, 154229.
41 A. Bahadoran, S. Masudy-Panah, J. R. De Lile, J. Li, J. Gu, B. Sadeghi, S. Ramakrishna and Q. Liu, *Int. J. Hydrogen Energy*, 2021, **46**, 24094–24106.
42 J. H. Pan and W. I. Lee, *Chem. Mater.*, 2006, **18**, 847–853.
43 L. Jiang, J. Wang, X. Wu and G. Zhang, *Water, Air, Soil Pollut.*, 2017, **228**(12), DOI: **10.1007/s11270-017-3646-4**.
44 P. Cai, S. M. Zhou, D. K. Ma, S. N. Liu, W. Chen and S. M. Huang, *Nano–Micro Lett.*, 2015, **7**, 183–193.
45 B. Li, C. Lai, G. Zeng, L. Qin, H. Yi, D. Huang, C. Zhou, X. Liu, M. Cheng, P. Xu, C. Zhang, F. Huang and S. Liu, *ACS Appl. Mater. Interfaces*, 2018, **10**, 18824–18836.
46 S. Dong, X. Ding, T. Guo, X. Yue, X. Han and J. Sun, *Chem. Eng. J.*, 2017, **316**, 778–789.
47 J. Liu, B. Wang, Z. Li, Z. Wu, K. Zhu, J. Zhuang, Q. Xi, Y. Hou, J. Chen, M. Cong, J. Li, G. Qian and Z. Lin, *J. Alloys Compd.*, 2019, **771**, 398–405.
48 R. Ameta, A. K. Chohadia, A. Jain and P. B. Punjabi, *Fenton and Photo-Fenton Processes*, 2018, DOI: **10.1016/B978-0-12-810499-6.00003-6**.
49 K. O'Dowd and S. C. Pillai, *J. Environ. Chem. Eng.*, 2020, **8**, 104063.
50 M. Liu, L. Zhang, B. D. Xi, S. Yu, X. Hu and L. A. Hou, *RSC Adv.*, 2017, **7**, 51512–51520.
51 V. D. Cao, L. X. Nong, V. H. Nguyen, T. V. Tran, H. T. Vu, C. V. Nguyen and S. T. Do, *IOP Conf. Ser.:Mater. Sci. Eng.*, 2020, **736**, 042019.
52 X. Ao and W. Liu, *Chem. Eng. J.*, 2017, **313**, 629–637.
53 Q. Zhao, Q. Mao, Y. Zhou, J. Wei, X. Liu, J. Yang, L. Luo, J. Zhang, H. Chen, H. Chen and L. Tang, *Chemosphere*, 2017, **189**, 224–238.
54 U. Ushani, X. Lu, J. Wang, Z. Zhang, J. Dai, Y. Tan, S. Wang, W. Li, C. Niu, T. Cai, N. Wang and G. Zhen, *Chem. Eng. J.*, 2020, **402**, 126232.
55 S. Guerra-Rodríguez, E. Rodríguez, D. N. Singh and J. Rodríguez-Chueca, *Water*, 2018, **10**(12), 1828.
56 C. Zhao, J. Wang, X. Chen, Z. Wang, H. Ji, L. Chen, W. Liu and C. C. Wang, *Sci. Total Environ.*, 2021, **752**, 141901.
57 K. Tian, F. Shi, M. Cao, Q. Zheng and G. Zhang, *Catalysts*, 2022, **12**(9), 1058.
58 C. Chen, Z. Wu, S. Zheng, L. Wang, X. Niu and J. Fang, *Environ. Sci. Technol.*, 2020, **54**(13), 8455–8463.
59 S. Li, H. Shang, Y. Tao, P. Li, H. Pan, Q. Wang, S. Zhang, H. Jia, H. Zhang, J. Cao, B. Zhang, R. Zhang, G. Li, Y. Zhang, D. Zhang and H. Li, *Angew. Chem., Int. Ed.*, 2023, **62**(28), e202305538.
60 X. Liu, S. Li, Z. Ren, H. Cao, Q. Yang, Z. Luo, L. He, J. Zhao, Q. Wang, G. Li, X. Liu, L. Chen, H. Li and D. Zhang, *Environ. Sci. Technol.*, 2024, **58**, 17797–17806.
61 K. Wang, Z. Guan, X. Liang, S. Song, P. Lu, C. Zhao, L. Yue, Z. Zeng, Y. Wu and Y. He, *Ultrason. Sonochem.*, 2023, **100**, 106616.